

Photon momentum-enabled electronic Raman scattering in silicon glass

Sergey S. Kharintsev^{1}, Elina I. Battalova¹, Aleksey I. Noskov^{1,2}, Jovany Merham², Eric O. Potma², and Dmitry A. Fishman^{2*}*

¹Department of Optics and Nanophotonics, Institute of Physics, Kazan Federal University,
Kazan 420008, Russia

²Department of Chemistry, University of California Irvine, Irvine, CA 92697, USA

skharint@gmail.com

dmitryf@uci.edu

Methods

Sample preparation

A modified Gatan Precision Ion Polishing System (PIPS, Gatan Inc.) was used as a sputter coater for a-Si thin film deposition on borosilicate microscopy cover slip (170 μm). Similar to Ref.¹, our modification of the PIPS enables coating of bulk sample surfaces and the deposition of thin films of a variety of materials. An advantage of using the PIPS for the latter purpose is the oil-free vacuum system, which allows films to be deposited with minimal carbon contamination. The sputter source was a piece of monocrystal wafer about 5 mm in diameter mounted on the standard specimen holder post. This milling system consists of two rare-earth Penning-type ion guns (PIGs), which were used together to speed up the sputtering process. The angle between guns and rotating target source material was +150 and did not change during the process. The system operated at the maximum acceleration voltage of 8 kV. The wafer source was sputter-cleaned for 2 minutes (pneumatic shutter in closed position) before the deposition process started. The vacuum level prior to deposition was typically 10^{-3} Pa or better. Typical sputtering times for producing amorphous thin films were in the range of 30 to 90 minutes, depending on the sputter source and thickness required.

Atomic force microscopy

The multimode scanning probe microscope Prima (NT-MDT) was utilized for visualizing the topography of the light-structured silicon glass samples. The AFM cantilever (VIT_P) was made of antimony-doped single crystal silicon (n-type, 0.01-0.025 Ohm-cm). The tip height was 14-16 μm , the tip curvature radius was 30 nm, and the resonant frequency was 300 kHz. For the height analysis, a 67% confidence (3σ) interval was used in Fig. 1 (e) and (f) (full range over heights).

Raman spectroscopy and microscopy

Raman spectra and maps were captured with a multi-purpose analytical instrument NTEGRA SPECTRA™ (NT-MDT) in the upright configuration. The confocal spectrometer was wavelength calibrated with a crystalline silicon (100) wafer by registering the first-order Raman band at 521 cm^{-1} . A sensitivity of the spectrometer was as high as ca. 1700 photon counts per 0.1 s when a $100\times$ objective (N.A.=0.7) was used, along with an exit slit (pinhole) of $100\text{ }\mu\text{m}$ and linearly polarized light with the wavelength of 632.8 nm . The illumination power at the sample was 10 mW . A Newton EMCCD camera (ANDOR) was employed without using the amplification option. Low-frequency Raman measurements were performed using a 633 nm Bragg notch filter (OptiGrate) with a spectral blocking window of 10 cm^{-1} . For spectral intensity analysis, a 95% confidence interval (2σ) was used, averaged over 10 points.

I. Light-structured a-Si film with 633 nm and 532 nm laser light

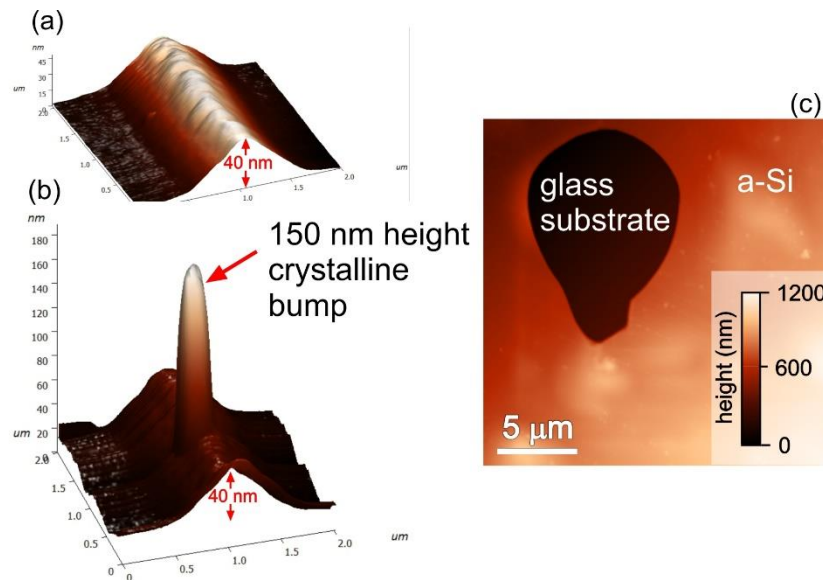


Figure SF1. (a) 3D AFM topography of light-structured a-Si ($16\text{ }\mu\text{m/s}$, 633 nm , 5 MW/cm^2), (b) 3D AFM topography of the same structure with a spot where a 532 nm laser with the intensity of 340 kW/cm^2 was on during 10 sec , (c) 2D AFM topography of a-Si film explosion under cw 532 nm illumination with an intensity of 1 MW/cm^2 .

II. Electron thermalization model

Here we explore a conventional emission model based on phonon-assisted fluorescence of thermalized conduction electrons. To understand the effects that different nanocrystal size distributions have on l -ERS and h -ERS, we start by considering the energy band structure for a glass system comprised of nanocrystalline c-Si embedded in an amorphous a-Si matrix (Figure 2b). The electronic energy of amorphous semiconductors $E_{\Delta}^a(\omega)$ for the given confinement Δ is calculated as a sum of its crystalline counterpart $E_{\Delta}^c(\omega)$ weighted by Lorentzian oscillators:²

$$E_{\Delta}^a(\omega) = \frac{1}{\pi} \int E_{\Delta}^c(\omega' + g_{\Delta}) \frac{\Gamma_{\Delta}}{(\omega - \omega')^2 + \Gamma_{\Delta}^2} d\omega', \quad (1)$$

where g_{Δ} and Γ_{Δ} are the size-dependent bandgap and bandwidth. Summing over all possible confinements yields a spectrum: $E^a(\omega) = \sum_{\Delta} E_{\Delta}^a(\omega)$. In fact, Eq. 1 describes the heterogeneous broadening of the electronic bands, and it can be illustrated by the pink shaded area in Figure 2b, where the c-Si energy bands are depicted as solid curves. In line with this concept, incident photons will predominantly be absorbed in a-Si, followed by hot electron thermalization into either the amorphous matrix or crystalline inclusions. In the former scenario, non-radiative recombination gains prominence due to the smearing of the higher valence and lower conduction band states³. Meanwhile, in large c-Si structures, phonon-assisted PL becomes a viable option as a relaxation channel.

We first attempt to explain this phenomenon via electron thermalization (Figure 2b) in the conduction band using the known dispersion relation $\omega(\mathbf{k})$ of Si bulk (green curves in Figures 2c and 2d). The h -ERS intensity is calculated as follows⁴⁻⁶:

$$I_{\Delta}(\omega) = I(\omega_0) \int_{BZ} \eta(\mathbf{k}) \frac{|C(\mathbf{k}, \Delta)|^2}{[\omega - \omega(\mathbf{k})]^2 + (\Gamma/2)^2} \exp\left[-a|\mathbf{k} - \mathbf{k}_p|\right] d^3\mathbf{k}, \quad (2)$$

where $I(\omega_0)$ is a pumping intensity at excitation frequency ω_0 , $C(\mathbf{k}, \Delta)$ is a size-dependent coupling coefficient (oscillator strength), Γ is the width of an electronic state, and Δ is the spatial

confinement factor defined as π/k . The integration in Eq. 2 is carried out over the entire Brillouin zone. The oscillator strength $C(\mathbf{k}, \Delta)$ reflects the recombination rate of an electron-hole pair.

It is important to note that, in spatially confined systems, the process of thermalization in the conduction band can only take place through discrete steps in the momentum space. This effect becomes apparent as a consequence of the discretization of the original phonon bath spectrum when confined. Simply put, the smallest thermalization step in reciprocal space is dictated by the size of the structure.

Following this notion, we introduce a step function in k-space in Eq. (2) as follows:

$$\eta(k) = \sum_{i=1}^N \theta(k - k_i^*) - \theta(k - k_i^* - \Delta k), \quad (3)$$

where $\theta(\cdot)$ is the Heaviside step function, k_i^* is a set of momenta which are relevant to the structures of choice ($i = 1, \dots, N$, with N being the number of possible thermalization jumps), and Δk is the electron momentum uncertainty. To address significant decrease in overall vibrational density of states (v-DOS) for smaller structures, we multiply the integrand in Eq. (2) by the exponential function $\exp[-a|\mathbf{k} - \mathbf{k}_p|]$, where k_p is the electron momentum corresponding to the pumping energy and a is a lattice parameter.

Using the extended form of Eq. (2) for the electron thermalization model aided by discrete phonons, we can compute the redshift of h -ERS for the one-dimensional case ($\Gamma - X$) with $C(k, \Delta) \sim k$,⁷ $\Gamma = 2 \cdot 10^{14}$ Hz and $a = 0.54$ nm. In this context, we explore various scenarios, when single, multiple, or a variable amount of thermalization jumps can be taken into consideration. First, the calculated redshifts of h -ERS are depicted as green curves in Figure SF2c and SF2d using a model with a single thermalization step. Notably, a significant deviation is observed between the calculated values and the experimental data across different excitation wavelengths. Specifically, for the 633 nm excitation wavelength, the results diverge as the structure size

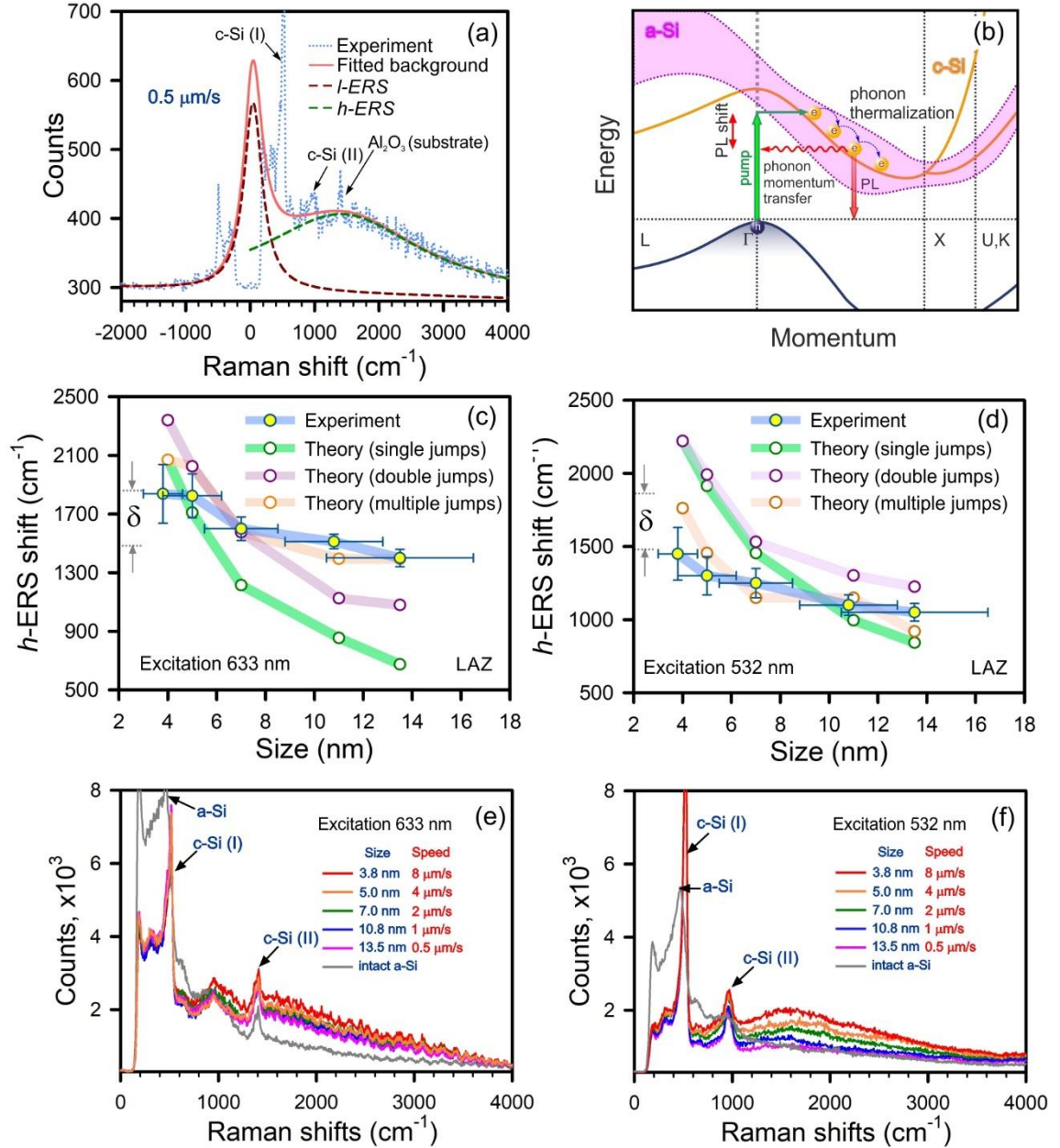


Figure SF2. (a) Raman spectrum at LAZ written at $0.5 \mu\text{m/s}$ (see also Figure 1c). The dashed curves are the l-ERS (red) and the h-ERS (green) extracted through spectrum analysis. (b) Schematic representation of electron thermalization on the conduction band, following indirect phonon-assisted luminescence. (c, d) Experimental data and theoretical model for red energy shift of h-ERS as a function of size for 633 nm (c) and 532 nm (d) excitations at LAZ. (e) and (f) Size-dependent Raman spectra for LAZ using exciting wavelengths 633 nm and 532 nm, respectively (exposure 10 s, pumping intensity 1.5 MW/cm^2).

increases, while for the 532 nm excitation, the discrepancies become more pronounced for smaller structures. We propose that these observations may be attributed to the slope of the dispersion

relation that affects the thermalization rate. Next, upon doubling the number of thermalization jumps for each size (depicted by magenta curves in Figures SF2c and SF2d), we observe a consistent upward shift in all curves, as expected. Further increase in the number of jumps results in a less satisfactory alignment with the experimental data. We note that quantum confinement not only leads to the discretization of the otherwise broad phonon spectrum of the bulk medium, but it also logically implies an overall decrease in the vibrational density of states. It is reasonable to expect that the number of thermalization jumps would be size-dependent. Finally, as can be seen from the plots (orange curves, Figures SF2c and SF2d), this consideration results in a close match between experimental data and theoretical model, with single jump used for 4 nm and up to 3 jumps for >10 nm structures. We note that quantum confinement not only leads to the discretization of broad phonon spectrum of bulk medium, but also logically implies an overall decrease in the vibrational density of states. It is reasonable to expect that the number of thermalization jumps would be a function of size. The optimal alignment between the model and experimental data was achieved by adjusting the number of jumps, as detailed in Table ST1. The slight variation in the number of steps for different excitation wavelengths can be attributed to the fact that shorter wavelengths facilitate the excitation of smaller structures.

Table ST1. Amount of steps used as a parameter for the thermalization model.

Structure size	633 nm	532 nm
3.8 nm	1	1
5 nm	2	1
7 nm	2	1
10.8 nm	3	2
13.5 nm	3	3

Despite its intuitive appeal, the process of electron thermalization followed by indirect phonon-assisted transitions falls short in explaining few crucial experimental observations. First, the energy shift of the emission remains constant for different excitation energies, *indicating the Raman nature of the process* (Figure 2f). Second, the observation of the emission at a very large Stokes shift ($>3000\text{ cm}^{-1}$), emission's *heavy tail*, also cannot be accounted for in the context of electron thermalization via phonons. Previous studies has demonstrated that the duration of thermalization in nanoscale systems can increase by an order of magnitude due to a reduced vibrational density of states (v-DOS).^{8,9} In other words, v-DOS becomes negligible for structures beyond a few nm, reducing the probability of emitting or absorbing phonons that are crucial for both electron thermalization and indirect phonon-assisted transition to the valence band as illustrated in Figure SF2. Moreover, quantum confinement should raise the bottom edge of the conductance band at the Γ -X point of the Brillouin zone by 1 eV (Supplementary Figure SF3). This means that the 633 nm pump is insufficient to induce indirect optical transitions in such sub-nanometer structures.

III. Effect of quantum confinement on c-Si energy gap

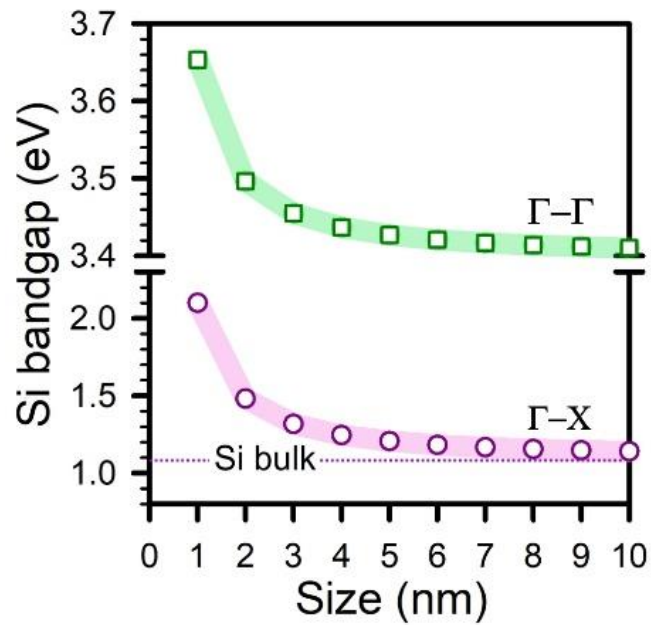


Figure SF3. A plot of the Si bandgap vs size for the $\Gamma-X$ and $\Gamma-\Gamma$ points of the Brillouin zone.¹⁰

IV. Emission at LAZ and HAZ from heterogeneous cross-linked silicon glass.

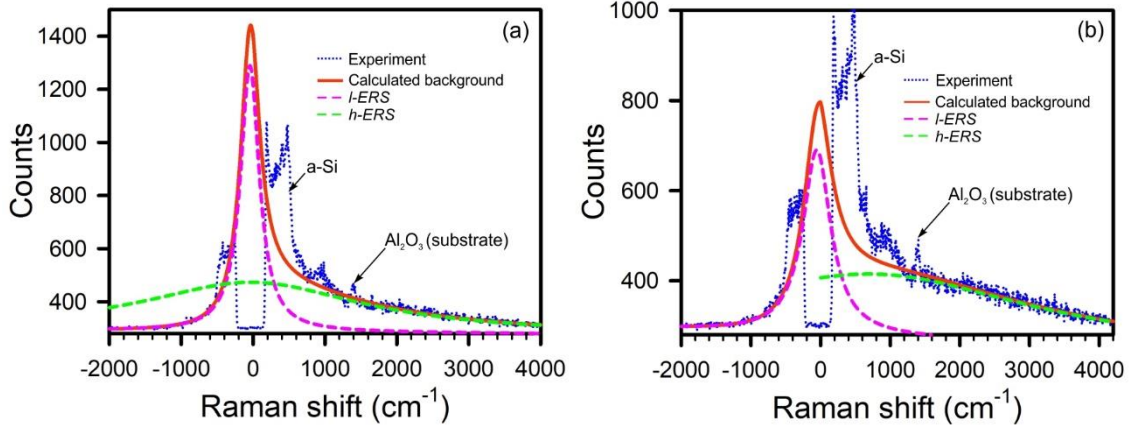


Figure SF4. Raman spectra of a-Si (a) and HAZ (b) and their numerical decomposition into *l*-ERS and *h*-ERS.

V. Optical density of states

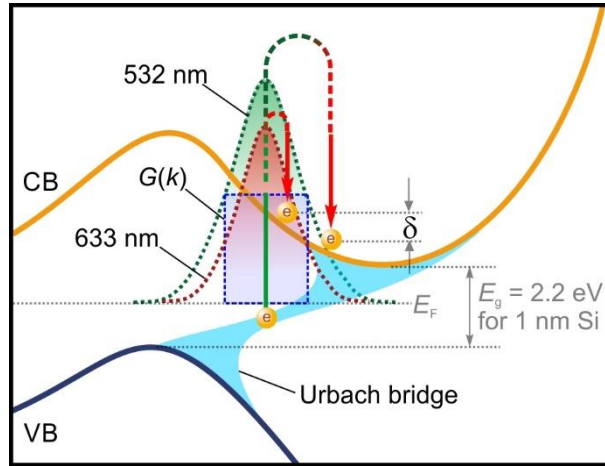


Figure SF5. Schematic of indirect optical transitions in a confined Si under 532 nm and 633 nm illumination. $G(k)$ is a function of momentum distribution.^{2,3}

While the width of the phonon's k -spectrum is entirely determined by the spatial nanostructure size in both cases, the confinement of a 532 nm photon is expected to lead to a higher optical density of states compared to the confinement of a 633 nm photon within the same structure. This inference directly arises from the density of states (DOS) of the original free photons, which scales as k^2 . By following the negative slope of the electronic dispersion between the Γ and X points, a higher amplitude k -spectrum at 532 nm results in a 400 cm^{-1} smaller average energy shift, as illustrated in Figure SF5.

VI. Light-structured metasurface

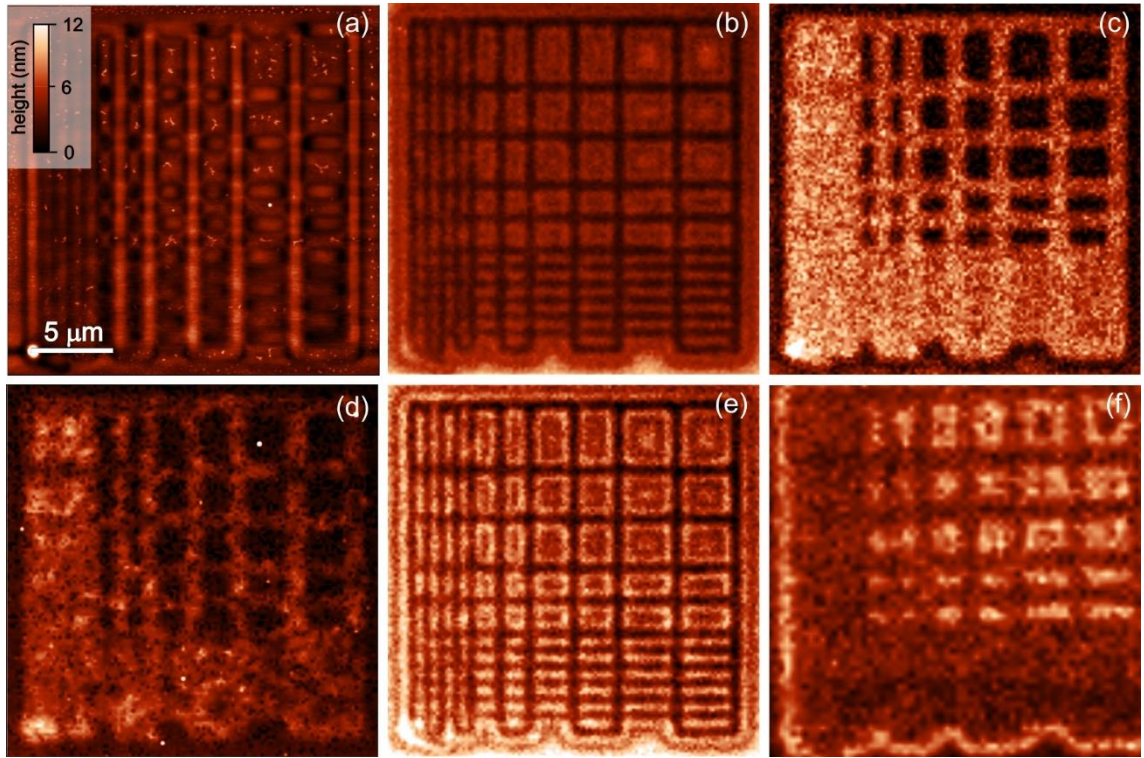


Figure SF6. Light-structured a-Si metasurface. (a) AFM topography, (b) Raman maps at 480 cm^{-1} (amorphous phase), (c) 521 cm^{-1} (crystalline phase), (d) at $600\text{-}3000\text{ cm}^{-1}$ (h -ERS), (e) 140 cm^{-1} (Boson peak), (f) $4000\text{-}5000\text{ cm}^{-1}$ (heavy h -ERS tail).

VII. Boson peak

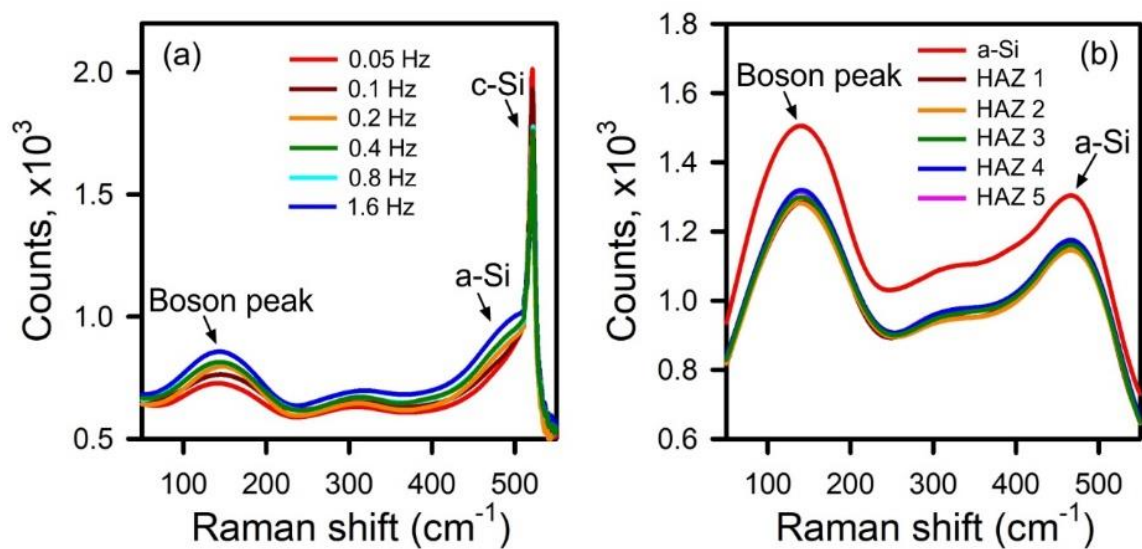


Figure SF7. Raman spectra of LAZ (a) and HAZ (b) for Si. The HAZs labelled as 1, 2, 3, 4, 5 correspond to the areas between the proper LAZs.

VIII. Raman mapping

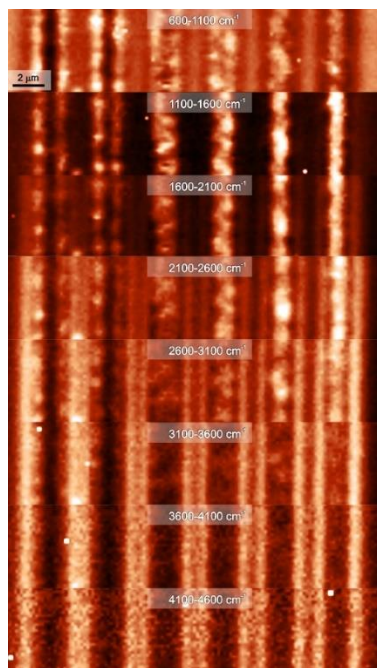


Figure SF8. The *h*-ERS map registered at different spectral regions.

IX. Heavy tail

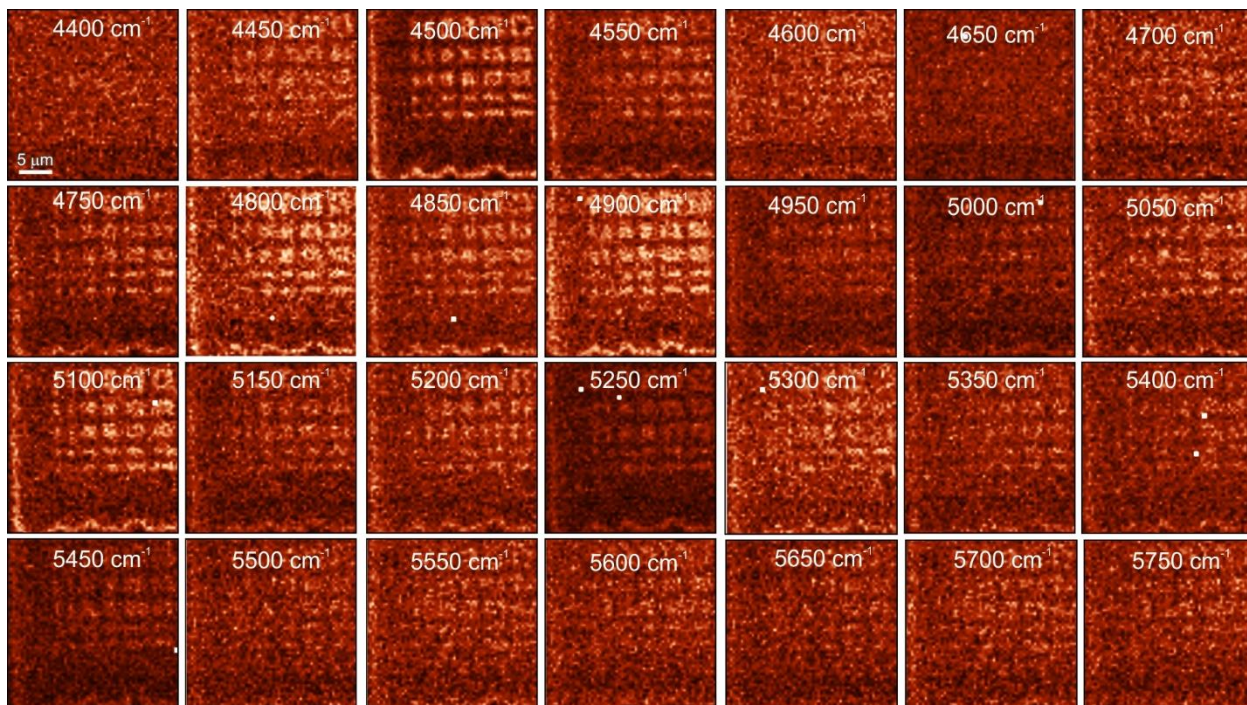


Figure SF9(a). Spectral Raman maps of the ERS heavy tail for 633 nm excitation.

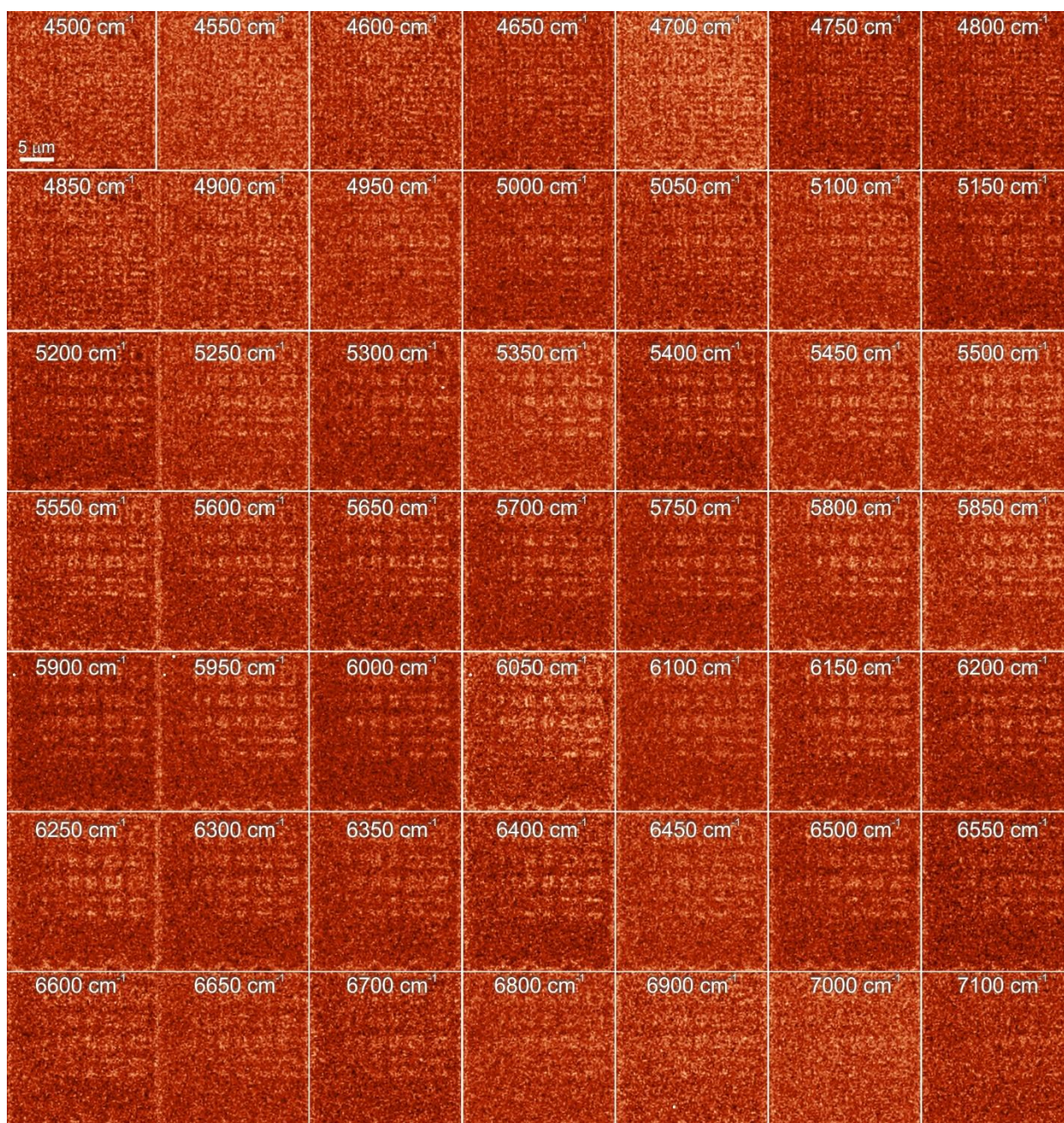


Figure SF9(b). A hyper-spectral Raman map of the ERS heavy tail for 532 nm excitation.

X. Pressure induced crystallization

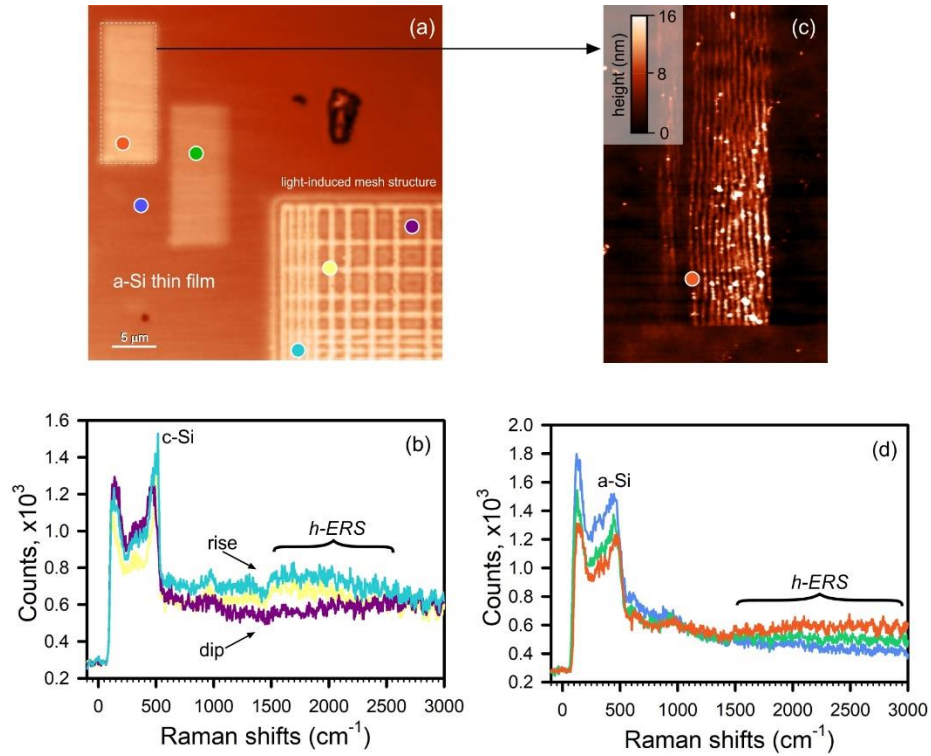


Figure SF10. (a) 2D confocal image of a light-structured a-Si film when a tip on (left top) and off (right bottom), (c) AFM topography of the highlighted area in Fig. SF9 (a), (b) and (d) Raman spectra at colorful spots in Fig. SF9 (a) (the color of curves corresponds to that of circles).

To demonstrate the effect from the pressure driven formations,¹¹ we conduct several exemplary experiments using an AFM cantilever in tapping mode. As shown in Figure SF10, we engraved a-Si film with light when the AFM cantilever in tapping mode was in (Fig. SF10a, rectangular with orange dot) and not in contact with the surface (Fig. SF10a, rectangular with green dot). In the first case, the *h*-ERS experience higher energy shifts (emission shifts to longer wavelengths), while the crystalline phase in the film composition is insignificant (no c-Si peak in Fig. SF10d).

References

- (1) G. J. C. Carpenter, Modification of a Gatan PIPS for thin-film deposition. *Microsc. Today* **22**, 36–39 (2014).
- (2) Ching, W. Y.; Lin, C. C.; Huber, D. L. Electronic Energy Structure of Amorphous Silicon. *Phys. Rev. B* **1976**, *14*, 620–631.
- (3) Kramer, B. Electronic Structure and Optical Properties of Amorphous Germanium and Silicon. *Phys. State Sol.* **1971**, *47*, 501–510.
- (4) Ben-Chorin, M.; Averboukh, B.; Kovalev, D.; Polisski, G.; Koch, F. Influence of Quantum Confinement on the Critical Points of the Band Structure of Si. *Phys. Rev. Lett.* **1996**, *77*, 763–766.
- (5) Spinella, C.; Lombardo, S.; Priolo, F. Crystal Grain Nucleation in Amorphous Silicon. *J. Appl. Phys.* **1998**, *84*, 5383–5414.